electronics

Article

Ship Detection in Spaceborne SAR Images under Radio Interference Environment Based on CFAR

Bengteng Ma †, Huizhang Yang † and Jian Yang *

Department of Electronic Engineering, Tsinghua University, Beijing 100084, China
* Correspondence: yangjian_ee@tsinghua.edu.cn
† These authors contributed equally to this work.

Abstract: Spaceborne synthetic aperture radar (SAR) can be easily interfered with by narrowband radio frequency interference (RFI) from ground radiation sources, causing significant degradation of image quality. In the application of SAR ship detection, the radio interference will raise the detection threshold of a constant false alarm rate (CFAR) detector, and consequently results in the degradation of detection performance. In order to solve this problem, we propose a ship-detection method for SAR under a narrowband RFI environment. The proposed method is mainly divided into five steps: (1) transform the input SAR image with narrowband RFI into 2-D frequency domain by fast Fourier transform (FFT); (2) use CFAR detector to detect RFI in 2-D frequency domain; (3) suppress RFI data points using adaptively weighting in the 2-D frequency domain; (4) transform the RFI suppressed 2-D spectrum into the image domain via inverse FFT; (5) apply CFAR detector for ship detection. Simulation and real data experiments show that the proposed method can effectively detect ships from SAR images with ocean background even if there exists serious RFI.

Keywords: spaceborne synthetic aperture radar; ship detection; radio frequency interference; constant false alarm rate detection

Citation: Ma, B.; Yang, H.; Yang, J. Ship Detection in Spaceborne SAR Images under Radio Interference Environment Based on CFAR. *Electronics* **2022**, *11*, 4135. https://doi.org/10.3390/electronics11244135

Academic Editor: Gwanggil Jeon

Received: 31 October 2022
Accepted: 6 December 2022
Published: 12 December 2022

1. Introduction

Spaceborne synthetic aperture radar (SAR) is an imaging radar mounted on an artificial earth satellite, which relies on the use of electromagnetic waves within microwave frequency bands (typically, from P band to Ka band). Because it is not limited by the lighting conditions, spaceborne SAR can perform all-day and all-weather earth observation, providing an important remote sensing tool in both civil and military applications [1,2].

However, the microwave spectrum is shared by different radio applications. When other types of radio equipment use the same frequency band as a SAR satellite, these equipments will cause potential RFI to the SAR satellite. The C/X band with the center frequency of about 5.4 GHz and 9.6 GHz and the bandwidth of less than 300 MHz is often used for spaceborne SAR. Due to spectrum sharing, these SARs are faced with radio frequency interference (RFI). Up to now, such interference has been observed by many SAR sensors, such as sentinel-1A/B, Radarsat-2, RCM constellation, and Gaofen-3 [3–6]. L band interference was also reported in ALOS POLSAR observation [7]. These interferences will greatly deteriorate the image quality of spaceborne SARs, causing difficulties for many down-stream applications, one of which is SAR ship detection.

Ship detection is an important application of SAR. Researchers have proposed many methods for this task, e.g., deep learning based detectors [8–11], superpixel detectors [12–15], polarimetric SAR detectors [16–21] and constant false alarm rate (CFAR) detectors [22–25]. These methods are effective if the SAR image is clean, however, if the SAR images are corrupted by RFI, these methods will have performance degradation and even fail. In order to suppress RFI in SAR for subsequent information retrieval, a number of signal-processing methods have been proposed for RFI detection [26–29] and removal [28,30–36]. According to the RFI bandwidth, RFI removal methods can be divided into narrowband

and wideband RFI suppressing methods. Narrowband RFI suppressing methods include notch filtering, eigen subspace filtering, etc. [34,37,38]. Wideband ones include frequency-domain notch filtering and improved eigen subspace filtering [39,40]. It is also notable that many optimization-based methods have been proposed in recent years [28,41–46]. Deep learning-based methods are also reported [47,48]. These RFI suppressing methods perform signal processing on SAR raw data to filter out RFI. For the focused SAR image, the above methods based on raw data processing are not applicable. Then, for such polluted SAR images, it will be difficult to apply for ship detection applications.

In this paper, we proposed a simple yet efficient processing flow for ship detection from SAR images acquired under narrowband RFI environment based on CFAR, where the CFAR module is used for both RFI removal and ship detection. The processing flow consists of five steps: (1) 2-D fast Fourier transform (FFT), (2) CFAR detection of RFI, (3) adaptive 2-D spectrum weighting, (4) 2-D inverse FFT (IFFT), (5) CFAR detection of ships. The steps 1–4 are used to suppress RFI to obtain a relatively clean SAR image, and the last step is to perform ship detection from the clean image. Simulation and real data experiments show that the proposed method can effectively improve SAR ship detection performance under narrowband RFI environments.

2. Signal Model

In the presence of RFI, the signal model of SAR received signal can be expressed as the summation of three terms, i.e.,

$$S(t_a, t_r) = S_{\text{scat}}(t_a, t_r) + J(t_a, t_r) + N(t_a, t_r) \tag{1}$$

where the three terms at the right of this equation denotes backscattered target echo, RFI, and noise respectively, and (t_a, t_r) is the fast time and slow time variables. For narrowband RFI, its signal model can be expressed as the sum of several sinusoids,

$$J(t_a, t_r) = \sum_k a_k(t_a) \exp(j2\pi f_k t_r) \tag{2}$$

The 2-D spectrum of the echo backscattered by a point target can be expressed as

$$S_{\text{scat,2df}}(f_a, f_r) = W_r(f_r) W_a(f_a - f_c) \exp\{j\theta_{\text{2df}}\} \tag{3}$$

where $S_{\text{2df}}(f_a, f_r)$ is 2-D Fourier transform of $S_{\text{scat}}(t_a, t_r)$. The transformation of SAR raw data into a SAR image can be regarded as matched filtering (MF) operation, which can be modelled by multiplication by a MF function $H(f_a, f_r)$ in the 2-D frequency domain, i.e.,

$$\begin{aligned} \tilde{S}(t'_a, t'_r) &= FT^{-1}\{FT\{S(t_a, t_r)\{\cdot H(f_a, f_r)\} \\ &= Q\{S_{\text{scat}}(t_a, t_r)\} + Q\{J(t_a, t_r)\} + Q\{N(t_a, t_r)\} \\ &= \tilde{S}_{\text{scat}}(t'_a, t'_r) + \tilde{J}(t'_a, t'_r) + \tilde{N}(t'_a, t'_r) \end{aligned} \tag{4}$$

where $Q\{\cdot\} = FT^{-1}\{FT\{\cdot\{\cdot H(f_a, f_r)\}$ is the matched filter. This fact shows that the bandwidth of $J(t_a, t_r)$ is preserved in $\tilde{J}(t'_a, t'_r)$, so we can still use narrowband signal model to describe $\tilde{J}(t'_a, t'_r)$, i.e.,

$$\tilde{J}(t'_a, t'_r) = \sum_k a'_k(t'_a) \exp(j2\pi f_k t'_r) \tag{5}$$

Therefore, we can use narrowband notch filtering to suppress RFI for subsequent ship detection in the SAR image. Although in SAR focusing algorithms the matched filter is spatially varying, the frequency band of RFI is still preserved in focused SAR images.

3. Ship Detection in SAR Images under RFI Environment

In the section, we introduce each step of our processing flow for ship detection from SAR images acquired under RFI environment.

3.1. Step 1: 2-D FFT

The first step is applying 2-D FFT to the SAR image,

$$\begin{aligned}\tilde{S}_{\mathrm{2df}}(f_a,f_r) =&\tilde{S}_{\mathrm{scat,2df}}(f_a,f_r)+\tilde{N}_{\mathrm{2df}}(f_a,f_r)+\int \tilde{J}(t_a,t_r)\exp(-j2\pi f_a t_a - jf_r t_r)dt_a \\ =&S_{\mathrm{scat,2df}}(f_a,f_r)+\tilde{N}_{\mathrm{2df}}(f_a,f_r) \\ &+\sum_k T\mathrm{sinc}(\pi T(f_r-f_k))\int a_k(t_a)\exp(-j2\pi f_a t_a)dt_a\end{aligned} \tag{6}$$

where $\mathrm{sinc}(x) = \sin(\pi x)/\pi x$. The sinc function in the last line of this equation, $\mathrm{sinc}(T(f_r - f_k))$, shows that the RFI in the 2-D frequency domain is a combination of several narrow responses. The total spectral occupation of the RFI, is thus the union of all the k bands,

$$B_{rfi} = \bigcup_k [f_k - 1/T, f_k + 1/T] \tag{7}$$

If the RFI energy is a few dB higher than the signal plus noise term, i.e., $S_{\mathrm{scat,2df}}(f_a,f_r) + \tilde{N}_{\mathrm{2df}}(f_a,f_r)$, the RFI will form a bright line in the 2-D spectral domain, and thus can be detected using CFAR as discussed in step 2.

3.2. Step 2: CFAR Detection of RFI

Considering the ocean environment, the backscattering coefficient is close to Gaussian clutter due to the speckle effect, and therefore the backscattering image spectrum, $\tilde{S}_{\mathrm{scat,2df}}(f_a,f_r)$, can be modelled as a Gaussian spectrum. In practice, SAR image spectrum of distributed scattering scenes usually can be viewed as a white Gaussian signal. Further considering that the noise spectrum is also white Gaussian, the detection of RFI in the 2-D spectral domain can be viewed as the problem of detecting a signal in the background of white Gaussian noise.

This can be achieved via CFAR detection, which perform adaptive binary thresholding using local clutter level estimate. This process can be described as follows,

$$M_1(f_a,f_r) = \begin{cases} 1, & \text{if } |\tilde{S}_{\mathrm{2df}}(f_a,f_r)|^2 > \alpha_1 T_1(f_a,f_r); \\ 0, & \text{otherwise.} \end{cases} \tag{8}$$

where $M_1(f_a,f_r)$ indicates whether (f_a,f_r) is decided to be a RFI frequency point, α is a scalar multiplier used to achieve desired probability of false alarm P_{fa}, and $\sigma^2(f_a,f_r)$ is the estimate of local clutter spectral level. For the standard CFAR, $T_1(f_a,f_r)$ is obtained via averaging N_1 samples of $|\tilde{S}_{\mathrm{2df}}(f_a,f_r)|^2$ selected around (f_a,f_r) using a sample window

$$T_1(f_a,f_r) = \frac{1}{N_1}\sum_k |\tilde{S}_{\mathrm{2df}}(f_a+x_k, f_r+y_k)|^2, \quad (x_k,y_k) \in H_1 \tag{9}$$

where H_1 is a window consisting of pixel offset of local spectrum samples to the center sample. The multiplier is determined by P_{fa} and N_1, which is given by $\alpha_1 = N_1(P_{\mathrm{fa},1}^{-1/N_1} - 1)$.

3.3. Step 3: Adaptive RFI Weighting

Let us denote the set of frequency points detected to have RFI as Ω_{rfi}. For each frequency point in this set, i.e., $(f_a,f_r) \in \Omega_{rfi}$, the signal model can be simply rewritten as

$$\tilde{S}_{\mathrm{2df}} = \tilde{S}_{\mathrm{scat,2df}} + \tilde{N}_{\mathrm{2df}} + \tilde{J}_{\mathrm{2df}} \tag{10}$$

For the reconstruction of $\tilde{S}_{\mathrm{scat,2df}}$, the linear estimation can be used via multiplying by a weighting variable $W_1(f_a,f_r)$, i.e.,

$$\hat{\tilde{S}}_{\mathrm{scat,2df}} = W_1 \tilde{S}_{\mathrm{2df}}. \tag{11}$$

The estimation error is then given as

$$J = E|W_2\tilde{S}_{\mathrm{2df}} - \tilde{S}_{\mathrm{scat,2df}}|^2 \tag{12}$$

where E denotes statistical expectation. Under the minimum square error criteria, the optimal W_2 is given as

$$W_1(f_a, f_r) = \underset{W_1}{\operatorname{argmin}}\, J = \frac{E|\tilde{S}_{\mathrm{scat,2df}}(f_a, f_r)|^2}{E|\tilde{S}_{\mathrm{2df}}(f_a, f_r)|^2} \tag{13}$$

for $(f_a, f_r) \in \Omega_{rfi}$, and $W_1(f_a, f_r) = 1$ for $(f_a, f_r) \notin \Omega_{rfi}$. We can approximate W_1 using the following approximation,

$$\tilde{S}_{\mathrm{scat,2df}}(f_a, f_r) = \sigma^2(f_a, f_r) \tag{14}$$

$$E|\tilde{S}_{\mathrm{2df}}(f_a, f_r)|^2 \approx |\tilde{S}_{\mathrm{2df}}(f_a, f_r)|^2 \tag{15}$$

where the first equation is the local approximation used in CFAR, and the second equation is a one-shot approximation.

An alternative weight is the following 0–1 weight,

$$W_2(f_a, f_r) = \begin{cases} 0, & \text{if exist } (\nu, \xi) \in \mathcal{N}_\Delta(f_a, f_r), \text{ s.t. } M_1(\nu, \xi) = 1; \\ 1, & \text{otherwise.} \end{cases} \tag{16}$$

where $\mathcal{N}_\Delta(f_a, f_r) = \{(\nu, \xi) | \nu \in [f_a - \Delta, f_a + \Delta], \xi \in [f_r - \Delta, f_r + \Delta]\}$ is the neighbourhood of (f_a, f_r). This masks out the any data point around detected the RFI frequency points with distance Δ in the 2-D frequency domain. It is notable that compared to other RFI suppressing methods, e.g., [49,50], the above weighting based method is simpler to implement.

In the following, we refer to (13) as weight 1 and (16) as weight 2, respectively.

3.4. Step 4: IFFT

With the RFI being suppressed or masked out in the 2-D spectrum, i.e., $\tilde{S}_{\mathrm{2df}}(f_a, f_r) \cdot W(f_a, f_r)$, then an inverse FFT can be used to reconstruct the clean image

$$\hat{\tilde{S}}(t'_a, t'_r) = \mathcal{F}^{-1}\{\tilde{S}_{\mathrm{2df}}(f_a, f_r) \cdot W(f_a, f_r)\} \tag{17}$$

Doing so, we can reconstruct a clean SAR image in which the RFI is suppressed.

3.5. Step 5: CFAR Ship Detection

At last, CFAR can be used to detect ships in the clean SAR image, which can be expressed as follows

$$M_2(f_a, f_r) = \begin{cases} 1, & \text{if } |\hat{\tilde{S}}(t'_a, t'_r)|^2 > \alpha_2 T_2(t'_a, t'_r); \\ 0, & \text{otherwise.} \end{cases} \tag{18}$$

where M_2 is the binary pixel-wise ship detection result, $\alpha_2 = N_2(P_{\mathrm{fa,2}}^{-1/N_2} - 1)$ is a scalar multiplier used to achieve a desired probability of false alarm $P_{\mathrm{fa,2}}$, and T_2 is the clutter estimate defined as follows

$$T_2(t'_a, t'_r) = \frac{1}{N_2} \sum_k |\hat{\tilde{S}}(t'_a + x_k, t'_r + y_k)|^2, \quad (x_k, y_k) \in H_2 \tag{19}$$

where H_2 is a window consisting of pixel offset of clutter samples to the center sample.

Based on the above, we provide the full processing flow in Figure 1. From this diagram, we can see that the processing flow is very simple and thus has the benefit of easy implementation, which only main involves two function-modules, i.e., FFT/IFFT module and CFAR module.

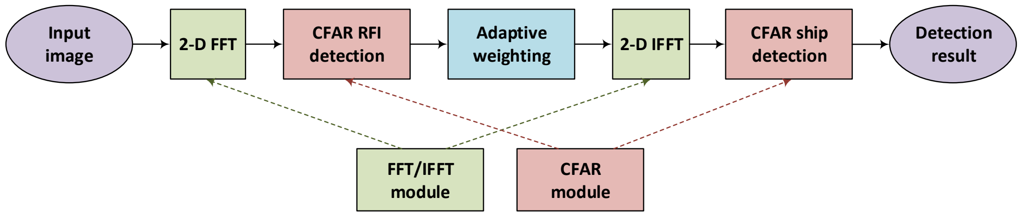

Figure 1. The processing flow for ship detection from SAR image acquired under a narrowband RFI environment.

4. Experiments

In this section, we use both simulated and real data to show the effectiveness of the proposed algorithm for SAR ship detection under a narrowband RFI environment. The performance of the algorithm is evaluated via the following metrics. The first metric is given as

$$Q_d = \frac{TP}{TP + TN}, \tag{20}$$

where TP and TN denotes, respectively, the number of positive and negative detection of pixels in the labeled box of ships. This metric is the percentage of correctly detected pixels to the label box of ships, which can be viewed as the pixel-wise detection rate of the labeled pixels. The second metric is defined as follows

$$Q_{fa} = \frac{FP}{FP + FN}, \tag{21}$$

where TP and TN denote, respectively, the number of positive and negative detections of pixels outside the labeled box of ships. This metric is the percentage of correctly detected pixels to the label box of ships, which can be viewed as the pixel-wise false alarm rate of the labeled pixels.

4.1. Experiment Using Simulated Data

In this experiment, we use a RFI-free Gaofen-3 SAR image with a ship as the clean images, and manually add simulated RFI artefacts to this image. The image is a 800×800 patch extracted from a Gaofen-3 fine-stripmap 2 HH image acquired on 20 January 2018 around (E19.7, N58.3). The sampling bandwidth of SAR is 66.6 MHz, and the RFI bandwidth is 1 MHz. The simulated RFI-polluted image is shown in Figure 2a, where range direction is horizontal and azimuth direction is vertical.

To better show the processing steps in the proposed method, we provide several images of data flows of this experiment in Figure 2b–f. Figure 2b is the 2-D image spectrum, which is obtained after the first step of the proposed algorithm. The bright vertical strip is the simulated narrowband RFI. Figure 2c is the CFAR detection results of RFI data point in the 2-D frequency domain, which is obtained after the second step of the proposed algorithm. Bright pixels denote positive detection results. Figure 2d is the weighted 2-D spectrum using the proposed adaptive weight in step 3. After this step, we can see that most RFI data are effectively suppressed in the 2-D spectrum. Figure 2e is the output clean image obtained by applying IFFT to the weighted spectrum in step 4. In this image, we can see that most RFI artefacts are now significantly suppressed. Figure 2f is the is the CFAR detection results of ships from the clean image, where bright pixels are positive detection results, which correspond to the ship and outliers.

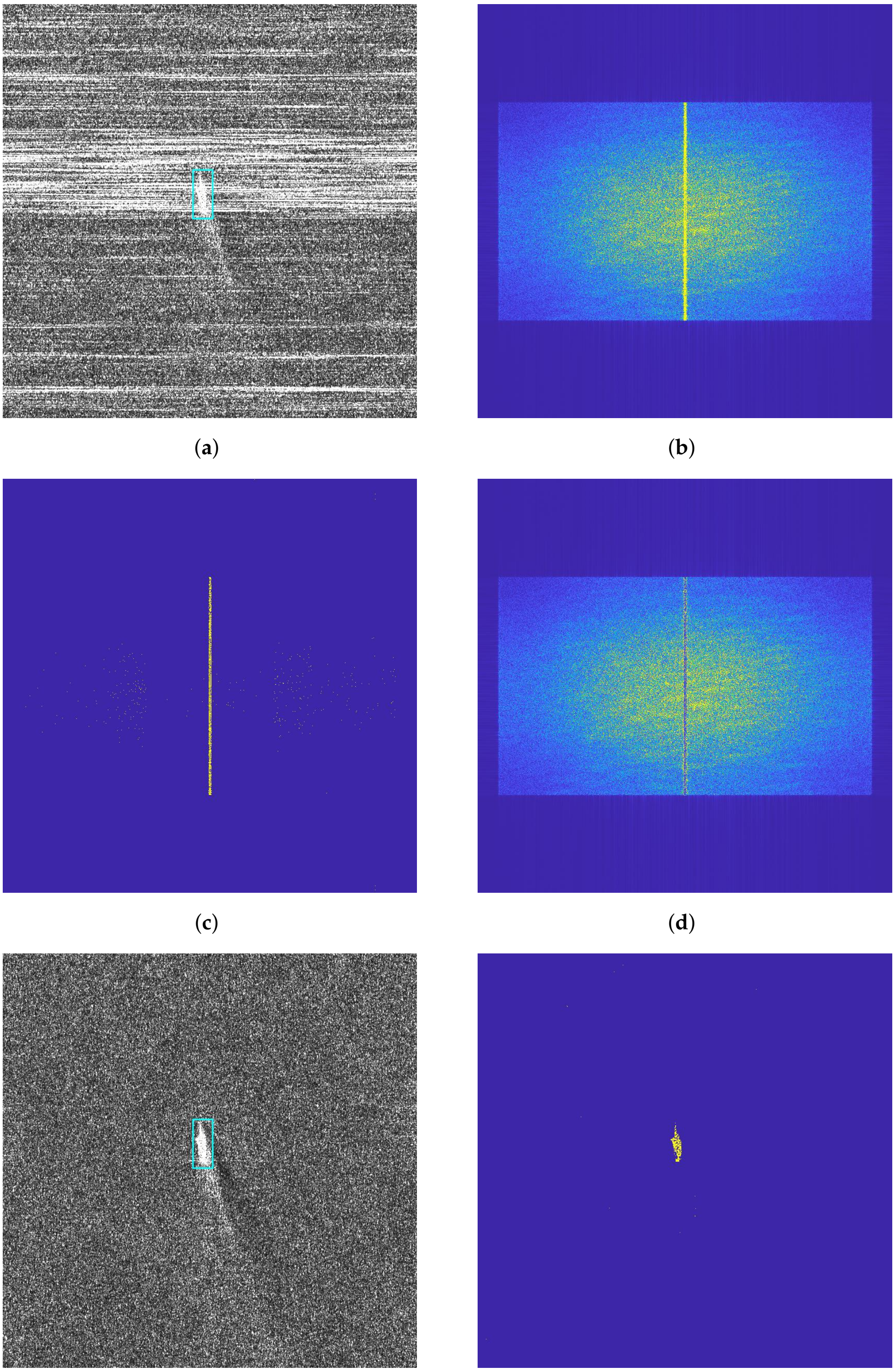

(**a**) (**b**) (**c**) (**d**) (**e**) (**f**)

Figure 2. Images in the processed steps of the first experiment. (**a**) SAR image plus simulated RFI; (**b**) Image 2-D spectrum; (**c**) CFAR detection of RFI from the 2-D spectrum; (**d**) Weighted 2-D spectrum; (**e**) Output clean image; (**f**) CFAR detection of ship from the clean image.

4.2. Experiments Using Real Data

In this experiment, we use Gaofen-3 SAR image acquired under a narrowband RFI environment. The image is a 2000×1000 patch extracted from a Gaofen-3 fine-stripmap 2 HH image acquired on 13 February 2019 around (E129.3, N31.9). The sampling bandwidth of SAR is 66.6 MHz, and the RFI band consists of several discontinuous bands less than 1 MHz. This experiment image and associated data flow in the processing steps are visualized in Figure 3a–f.

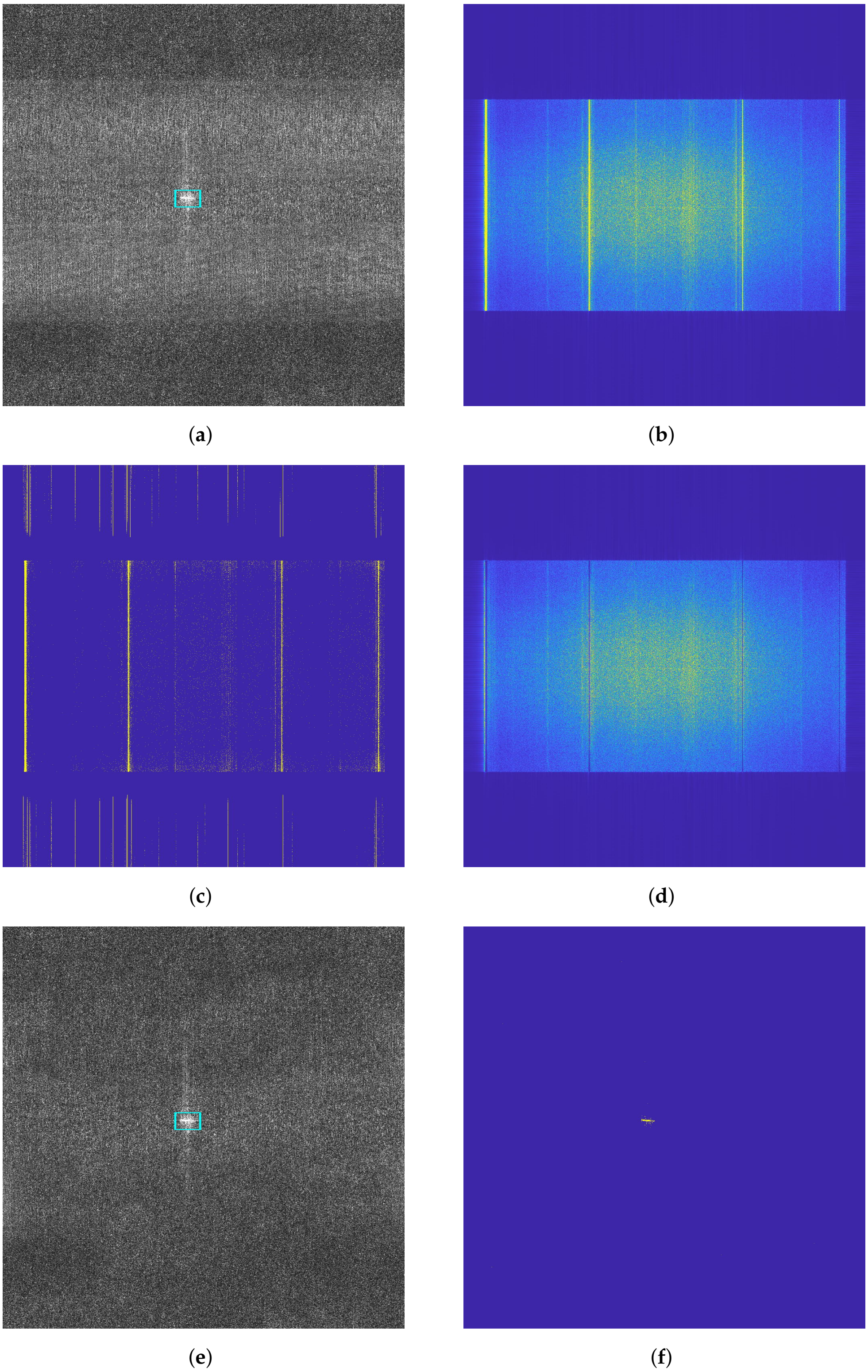

Figure 3. Images in the processed steps of the second experiment. (**a**) SAR image; (**b**) Image 2-D spectrum; (**c**) CFAR detection of RFI from the 2-D spectrum (**d**) Weighted 2-D spectrum; (**e**) Output clean image; (**f**) CFAR detection of ship from the clean image.

4.3. Quantitative Analysis

In order to quantitatively evaluate the performance of the proposed algorithm, we calculate $Q_d - Q_{fa}$ curves for four different experiment images, which are shown in Figure 4. The first and second images are those shown in Figures 2a and 3a, respectively, and the third and fourth images are given in Figure 5a,b, respectively. The curve of $Q_d - Q_{fa}$ obtained without spectrum weighting are compared with that obtained using two weighting method discussed in the previous section.

In Figure 4a,d, we can see that the proposed algorithm, using either weight 1 or weight 2, can effectively improve the detection performance in terms of higher Q_d, i.e., the ratio of correctly detected pixels in the label box. For example, in Figure 4d, Q_d obtained via using weight 1 and weight 2 are 0.5 and 0.14 higher than that obtained without using spectrum weighting.

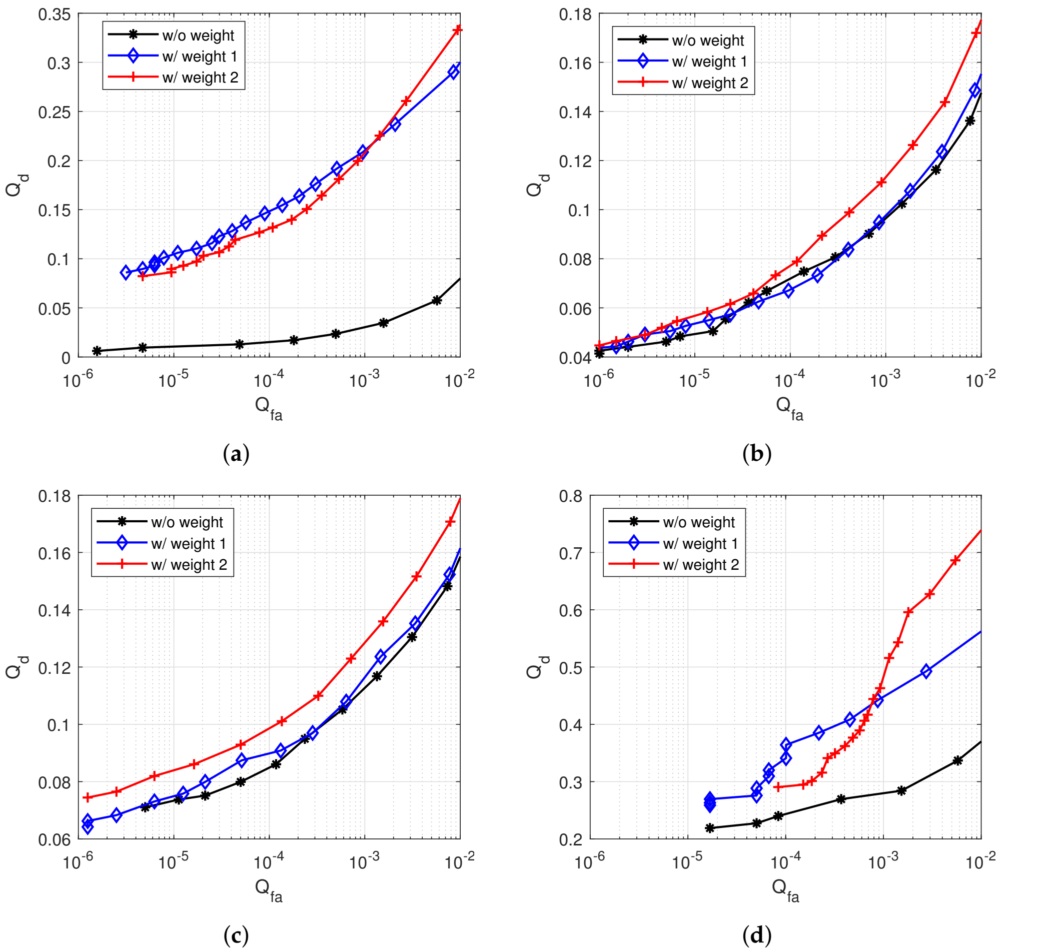

Figure 4. Curves of $Q_d - Q_{fa}$ obtained from four experiments. (**a**) Experiment 1; (**b**) experiment 2; (**c**) experiment 3; (**d**) experiment 4.

In Figure 4b,c, Q_d obtained via using weight 2 is always higher than that obtained without using spectrum weighting. However, this does not hold for that obtained using weight 1. This implies that weight 2 is more robust than weight 1.

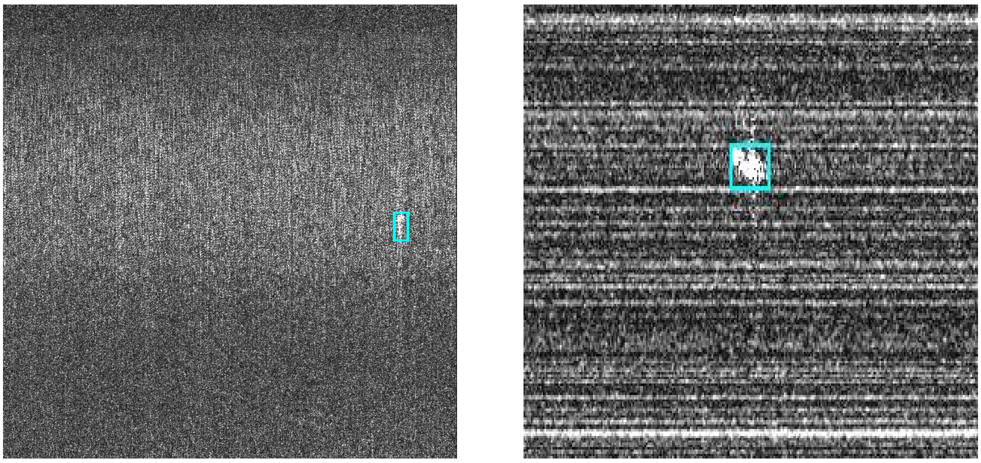

(a) (b)

Figure 5. The third and fourth images for quantitative analysis, which contain narrowband RFI. (**a**) Sentinel-1 image, (**b**) Gaofen-3 image.

5. Conclusions

In this paper, we proposed an efficient processing flow for ship detection in SAR images under a narrowband RFI environment. First, we formulate an SAR received signal model containing narrowband RFI, and we use matched filtering analysis to show that the RFI is also narrowband in the image domain. Then, we propose a CFAR based processing flow for ship detection in SAR images under a narrowband RFI environment, which works in a manner of RFI removal followed by ship detection. The overall processing flow consists of five steps: (1) 2-D FFT, (2) CFAR detection of RFI, (3) adaptive 2-D spectrum weighting for RFI suppression, (4) 2-D IFFT, (5) CFAR detection of ships.

We test the effectiveness of the proposed method using both simulated data (real SAR image plus simulated RFI) and real data (Chinese Gaofen-3 spaceborne SAR image acquired under RFI environment). Experimental results show that the proposed method can effectively improve detection performance.

Author Contributions: Conceptualization, J.Y. and H.Y.; methodology, B.M. and H.Y.; software, B.M. and H.Y.; validation, B.M. and H.Y.; formal analysis, B.M. and H.Y.; investigation, B.M. and H.Y.; resources, B.M. and H.Y.; data curation, B.M. and H.Y.; writing—original draft preparation, B.M. and H.Y.; writing—review and editing, B.M., H.Y. and J.Y.; visualization, B.M. and H.Y.; supervision, J.Y.; project administration, J.Y.; funding acquisition, J.Y. All authors have read and agreed to the published version of the manuscript.

Funding: This work was partly supported by NSFC under Grant no. 2022M711873, 62222102, 62171023, and 2021TQ0165.

Acknowledgments: The authors would like to thank National Satellite Ocean Application Service (NSOAS) for providing the data free of charge.

Conflicts of Interest: The authors declare no conflict of interest.

Abbreviations

The following abbreviations are used in this manuscript:

SAR	Synthetic aperture radar
CFAR	Constant false alarm rate
RFI	Radio frequency interference
FFT	Fast Fourier transform

References

1. Moreira, A.; Prats-Iraola, P.; Younis, M.; Krieger, G.; Hajnsek, I.; Papathanassiou, K.P. A tutorial on synthetic aperture radar. *IEEE Geosci. Remote Sens. Mag.* **2013**, *1*, 6–43. [CrossRef]
2. Yunkai, D.; Weidong, Y.; Heng, Z.; Wei, W.; Dacheng, L.; Robert, W. Forthcoming spaceborne SAR development. *J. Radars* **2020**, *9*, 1–33.
3. Hajduch, G.; Le Levier, D. Mutual interference between C-band SAR. In Proceedings of the VH-RODA Workshop, Frascati, Italy, 18–22 November 2019.
4. Leng, X.; Ji, K.; Kuang, G. Radio Frequency Interference Detection and Localization in Sentinel-1 Images. *IEEE Trans. Geosci. Remote Sens.* **2021**, *59*, 9270–9281. [CrossRef]
5. Yang, H.; Tao, M.; Chen, S.; Xi, F.; Liu, Z. On the Mutual Interference Between Spaceborne SARs: Modeling, Characterization, and Mitigation. *IEEE Trans. Geosci. Remote Sens.* **2020**, *59*, 8470–8485. [CrossRef]
6. Li, N.; Zhang, H.; Lv, Z.; Min, L.; Guo, Z. Simultaneous Screening and Detection of RFI From Massive SAR Images: A Case Study on European Sentinel-1. *IEEE Trans. Geosci. Remote Sens.* **2022**, *60*, 1–17. [CrossRef]
7. Natsuaki, R.; Motohka, T.; Suzuki, S.; Tadono, T. Radio frequency interference in ALOS-2 PALSAR-2 interferogram. In Proceedings of the 2017 XXXIInd General Assembly and Scientific Symposium of the International Union of Radio Science (URSI GASS), Montreal, QC, Canada, 19–26 August 2017; pp. 1–4.
8. Wang, Y.; Wang, C.; Zhang, H.; Dong, Y.; Wei, S. A SAR dataset of ship detection for deep learning under complex backgrounds. *Remote Sens.* **2019**, *11*, 765. [CrossRef]
9. Cui, Z.; Wang, X.; Liu, N.; Cao, Z.; Yang, J. Ship detection in large-scale SAR images via spatial shuffle-group enhance attention. *IEEE Trans. Geosci. Remote Sens.* **2020**, *59*, 379–391. [CrossRef]
10. Ai, J.; Tian, R.; Luo, Q.; Jin, J.; Tang, B. Multi-scale rotation-invariant Haar-like feature integrated CNN-based ship detection algorithm of multiple-target environment in SAR imagery. *IEEE Trans. Geosci. Remote Sens.* **2019**, *57*, 10070–10087. [CrossRef]
11. Lang, P.; Fu, X.; Feng, C.; Dong, J.; Qin, R.; Martorella, M. LW-CMDANet: A Novel Attention Network for SAR Automatic Target Recognition. *IEEE J. Sel. Top. Appl. Earth Obs. Remote Sens.* **2022**, *15*, 6615–6630. [CrossRef]
12. Wang, X.; Li, G.; Plaza, A.; He, Y. Ship detection in SAR images via enhanced nonnegative sparse locality-representation of Fisher vectors. *IEEE Trans. Geosci. Remote Sens.* **2021**, *59*, 9424–9438. [CrossRef]
13. Yu, W.; Wang, Y.; Liu, H.; He, J. Superpixel-based CFAR target detection for high-resolution SAR images. *IEEE Geosci. Remote Sens. Lett.* **2016**, *13*, 730–734. [CrossRef]
14. Li, T.; Peng, D.; Chen, Z.; Guo, B. Superpixel-Level CFAR detector based on truncated gamma distribution for SAR images. *IEEE Geosci. Remote Sens. Lett.* **2020**, *18*, 1421–1425. [CrossRef]
15. Cui, Z.; Hou, Z.; Yang, H.; Liu, N.; Cao, Z. A CFAR target-detection method based on superpixel statistical modeling. *IEEE Geosci. Remote Sens. Lett.* **2020**, *18*, 1605–1609. [CrossRef]
16. Atteia, G.; Collins, M.J. On the use of compact polarimetry SAR for ship detection. *ISPRS J. Photogramm. Remote Sens.* **2013**, *80*, 1–9. [CrossRef]
17. Zhang, T.; Ji, J.; Li, X.; Yu, W.; Xiong, H. Ship detection from PolSAR imagery using the complete polarimetric covariance difference matrix. *IEEE Trans. Geosci. Remote Sens.* **2018**, *57*, 2824–2839. [CrossRef]
18. Cui, X.C.; Tao, C.S.; Su, Y.; Chen, S.W. PolSAR ship detection based on polarimetric correlation pattern. *IEEE Geosci. Remote Sens. Lett.* **2020**, *18*, 471–475. [CrossRef]
19. He, J.; Wang, Y.; Liu, H.; Wang, N.; Wang, J. A novel automatic PolSAR ship detection method based on superpixel-level local information measurement. *IEEE Geosci. Remote Sens. Lett.* **2018**, *15*, 384–388. [CrossRef]
20. Zhang, T.; Wang, W.; Quan, S.; Yang, H.; Xiong, H.; Zhang, Z.; Yu, W. Region-based polarimetric covariance difference matrix for PolSAR ship detection. *IEEE Trans. Geosci. Remote Sens.* **2022**, *60*, 1–16.
21. Zhang, T.; Quan, S.; Yang, Z.; Guo, W.; Zhang, Z.; Gan, H. A Two-Stage Method for Ship Detection Using PolSAR Image. *IEEE Trans. Geosci. Remote Sens.* **2022**, *60*, 5236918. [CrossRef]
22. Banerjee, A.; Burlina, P.; Chellappa, R. Adaptive target detection in foliage-penetrating SAR images using alpha-stable models. *IEEE Trans. Image Process.* **1999**, *8*, 1823–1831. [CrossRef]
23. Gao, G.; Shi, G. CFAR ship detection in nonhomogeneous sea clutter using polarimetric SAR data based on the notch filter. *IEEE Trans. Geosci. Remote Sens.* **2017**, *55*, 4811–4824. [CrossRef]
24. Liu, T.; Yang, Z.; Marino, A.; Gao, G.; Yang, J. Robust CFAR detector based on truncated statistics for polarimetric synthetic aperture radar. *IEEE Trans. Geosci. Remote Sens.* **2020**, *58*, 6731–6747. [CrossRef]
25. Leng, X.; Ji, K.; Yang, K.; Zou, H. A bilateral CFAR algorithm for ship detection in SAR images. *IEEE Geosci. Remote Sens. Lett.* **2015**, *12*, 1536–1540. [CrossRef]
26. Li, N.; Lv, Z.; Guo, Z. Observation and Mitigation of Mutual RFI Between SAR Satellites: A Case Study Between Chinese GaoFen-3 and European Sentinel-1A. *IEEE Trans. Geosci. Remote Sens.* **2022**, *60*, 1–19. [CrossRef]
27. Tao, M.; Li, J.; Chen, J.; Liu, Y.; Fan, Y.; Su, J.; Wang, L. Radio Frequency Interference Signature Detection in Radar Remote Sensing Image Using Semantic Cognition Enhancement Network. *IEEE Trans. Geosci. Remote Sens.* **2022**, *60*, 1–14. [CrossRef]
28. Li, N.; Lv, Z.; Guo, Z. Pulse RFI Mitigation in Synthetic Aperture Radar Data via a Three-Step Approach: Location, Notch, and Recovery. *IEEE Trans. Geosci. Remote Sens.* **2022**, *60*, 1–17. [CrossRef]

29. Lu, X.; Wang, C.; Xu, X.; Yang, H.; Zhang, S.; Tan, K.; Bao, X.; Su, W.; Gu, H. Automatic RFI Identification for Sentinel-1 Based on Siamese-Type Deep CNN Using Repeat-Pass Images. *IEEE Trans. Geosci. Remote Sens.* **2022**, *60*, 1–16. [CrossRef]
30. Tao, M.; Su, J.; Huang, Y.; Wang, L. Mitigation of radio frequency interference in synthetic aperture radar data: Current status and future trends. *Remote Sens.* **2019**, *11*, 2438. [CrossRef]
31. Ren, J.; Zhang, T.; Li, J.; Nguyen, L.H.; Stoica, P. RFI Mitigation for UWB Radar Via Hyperparameter-Free Sparse SPICE Methods. *IEEE Trans. Geosci. Remote Sens.* **2018**, *57*, 3105–3118. [CrossRef]
32. Wang, X.Y.; Yu, W.D.; Qi, X.Y.; Liu, Y. RFI suppression in SAR based on approximated spectral decomposition algorithm. *Electron. Lett.* **2012**, *48*, 594–596. [CrossRef]
33. Huang, Y.; Chen, Z.; Wen, C.; Li, J.; Xia, X.G.; Hong, W. An Efficient Radio Frequency Interference Mitigation Algorithm in Real Synthetic Aperture Radar Data. *IEEE Trans. Geosci. Remote Sens.* **2022**, *60*, 1–12. [CrossRef]
34. Xu, W.; Xing, W.; Fang, C.; Huang, P.; Tan, W. RFI suppression based on linear prediction in synthetic aperture radar data. *IEEE Geosci. Remote Sens. Lett.* **2020**, *18*, 2127–2131. [CrossRef]
35. Tao, M.; Lai, S.; Li, J.; Su, J.; Fan, Y.; Wang, L. Extraction and Mitigation of Radio Frequency Interference Artifacts Based on Time-Series Sentinel-1 SAR Data. *IEEE Trans. Geosci. Remote Sens.* **2021**, *60*, 1–11. [CrossRef]
36. Han, W.; Zhou, F. SAR Wideband Interference Suppression Method Using Second-Order Multisynchrosqueezing Transform. *IEEE Trans. Geosci. Remote Sens.* **2022**, *60*, 1–15. [CrossRef]
37. Meyer, F.J.; Nicoll, J.B.; Doulgeris, A.P. Correction and characterization of radio frequency interference signatures in L-band synthetic aperture radar data. *IEEE Trans. Geosci. Remote Sens.* **2013**, *51*, 4961–4972. [CrossRef]
38. Zhou, F.; Wu, R.; Xing, M.; Bao, Z. Eigensubspace-based filtering with application in narrow-band interference suppression for SAR. *IEEE Geosci. Remote Sens. Lett.* **2007**, *4*, 75–79. [CrossRef]
39. Zhang, S.; Xing, M.; Guo, R.; Zhang, L.; Bao, Z. Interference suppression algorithm for SAR based on time–frequency transform. *IEEE Trans. Geosci. Remote Sens.* **2011**, *49*, 3765–3779. [CrossRef]
40. Tao, M.; Zhou, F.; Zhang, Z. Wideband interference mitigation in high-resolution airborne synthetic aperture radar data. *IEEE Trans. Geosci. Remote Sens.* **2015**, *54*, 74–87. [CrossRef]
41. Huang, Y.; Liao, G.; Li, J.; Xu, J. Narrowband RFI suppression for SAR system via fast implementation of joint sparsity and low-rank property. *IEEE Trans. Geosci. Remote Sens.* **2018**, *56*, 2748–2761. [CrossRef]
42. Yang, H.; Chen, C.; Chen, S.; Xi, F.; Liu, Z. A Dictionary-Based SAR RFI Suppression Method via Robust PCA and Chirp Scaling Algorithm. *IEEE Geosci. Remote Sens. Lett.* **2020**, *18*, 1229–1233. [CrossRef]
43. Lu, X.; Yang, J.; Yu, W.; Su, W.; Gu, H.; Yeo, T.S. Enhanced LRR-Based RFI Suppression for SAR Imaging Using the Common Sparsity of Range Profiles for Accurate Signal Recovery. *IEEE Trans. Geosci. Remote Sens.* **2020**, *59*, 1302–1318. [CrossRef]
44. Huang, Y.; Zhang, L.; Yang, X.; Chen, Z.; Liu, J.; Li, J.; Hong, W. An efficient graph-based algorithm for time-varying narrowband interference suppression on SAR system. *IEEE Trans. Geosci. Remote Sens.* **2021**, *59*, 8418–8432. [CrossRef]
45. Lu, X.; Yang, J.; Yeo, T.S.; Su, W.; Gu, H.; Yu, W. Accurate SAR Image Recovery From RFI Contaminated Raw Data by Using Image Domain Mixed Regularizations. *IEEE Trans. Geosci. Remote Sens.* **2021**, *60*, 1–13. [CrossRef]
46. Zhang, H.; Min, L.; Lu, J.; Chang, J.; Guo, Z.; Li, N. An Improved RFI Mitigation Approach for SAR Based on Low-Rank Sparse Decomposition: From the Perspective of Useful Signal Protection. *Remote Sens.* **2022**, *14*, 3278. [CrossRef]
47. Fan, W.; Zhou, F.; Tao, M.; Bai, X.; Rong, P.; Yang, S.; Tian, T. Interference mitigation for synthetic aperture radar based on deep residual network. *Remote Sens.* **2019**, *11*, 1654. [CrossRef]
48. Tao, M.; Li, J.; Su, J.; Wang, L. Characterization and Removal of RFI Artifacts in Radar Data via Model-Constrained Deep Learning Approach. *Remote Sens.* **2022**, *14*, 1578. [CrossRef]
49. Yang, H.; He, Y.; Du, Y.; Zhang, T.; Yin, J.; Yang, J. Two-Dimensional Spectral Analysis Filter for Removal of LFM Radar Interference in Spaceborne SAR Imagery. *IEEE Trans. Geosci. Remote Sens.* **2021**, *60*, 1–16. [CrossRef]
50. Yang, H.; Li, K.; Li, J.; Du, Y.; Yang, J. BSF: Block Subspace Filter for Removing Narrowband and Wideband Radio Interference Artifacts in Single-Look Complex SAR Images. *IEEE Trans. Geosci. Remote Sens.* **2021**, *60*, 5211916. [CrossRef]